



**HAL**  
open science

# Correlation between microstructure and cyclic behavior of 316L stainless steel obtained by Laser Powder Bed Fusion

Xiaoyu Liang, Anis Hor, Camille Robert, Mehdi Salem, Franck Morel

► **To cite this version:**

Xiaoyu Liang, Anis Hor, Camille Robert, Mehdi Salem, Franck Morel. Correlation between microstructure and cyclic behavior of 316L stainless steel obtained by Laser Powder Bed Fusion. *Fatigue and Fracture of Engineering Materials and Structures*, 2022, 45 (5), pp.1505-1520. 10.1111/ffe.13684 . hal-03616357

**HAL Id: hal-03616357**

**<https://imt-mines-albi.hal.science/hal-03616357>**

Submitted on 30 Jun 2022

**HAL** is a multi-disciplinary open access archive for the deposit and dissemination of scientific research documents, whether they are published or not. The documents may come from teaching and research institutions in France or abroad, or from public or private research centers.

L'archive ouverte pluridisciplinaire **HAL**, est destinée au dépôt et à la diffusion de documents scientifiques de niveau recherche, publiés ou non, émanant des établissements d'enseignement et de recherche français ou étrangers, des laboratoires publics ou privés.

# Correlation between microstructure and cyclic behavior of 316L stainless steel obtained by Laser Powder Bed Fusion

Xiaoyu Liang<sup>1,2,3</sup>  | Anis Hor<sup>2</sup> | Camille Robert<sup>1</sup> | Mehdi Salem<sup>2</sup> | Franck Morel<sup>1</sup>

<sup>1</sup>Angers Laboratory of Mechanics, Manufacturing Process and Innovation (LAMPA), Arts et Métiers Campus Angers, Angers, France

<sup>2</sup>Institut Clément Ader (ICA), Université de Toulouse, CNRS, ISAE-SUPAERO, UPS, INSA, Toulouse, France

<sup>3</sup>Department of Mechanical Engineering, Tsinghua University, Beijing, China

## Correspondence

Anis Hor, Institut Clément Ader (ICA), Université de Toulouse, CNRS, ISAE-SUPAERO, UPS, INSA, Mines-Albi, 3 rue Caroline Aigle, 31400 Toulouse, France.  
Email: anis.hor@isae-supaeo.fr

## Abstract

In this work, stainless steel 316L obtained by Laser Powder Bed Fusion (L-PBF) has been produced and characterized. The experimental campaign focuses on the samples in the as-built state under cyclic tension-compression loadings. Low cycle fatigue (LCF) and high cycle fatigue (HCF) tests are carried out. Microstructure observations are performed before and after the loadings. As-built L-PBF 316L has a good LCF performance despite the presence of surface defects but a low fatigue limit in the HCF regime. Removing the surface roughness has a beneficial effect but does not improve the fatigue strength to that of machined wrought 316L. Observations on the microstructure of fatigue samples indicate that LCF is dominated by the local plastic deformation, which is mostly achieved by the slip in the studied material and is not sensitive to the defect. The lack-of-fusion defect impairs the fatigue resistance in the HCF regime.

## KEYWORDS

cyclic behavior, fatigue, Laser Powder Bed Fusion, stainless steel 316L, microstructure

## 1 | INTRODUCTION

Possessing a high mechanical strength combined with good corrosion resistance, stainless steels (SSs) have been indispensable metallic materials in many industrial fields. The 316L SS, due to the deliberate amount of molybdenum and the low proportion of carbon, offers better corrosion resistance, superior formability, and weldability as well as biocompatibility. This material has been widely applied to the petroleum industry, the nuclear industry, the medical field, and so on. In recent years, a fast-developed technique, additive manufacturing (AM), provides a new route for fabricating 316L SS.<sup>1–4</sup> Among the AM techniques, Laser Powder Bed Fusion (L-PBF) (also known as selective laser melting (SLM)) is very promising in preparing the metallic materials on its

excellent precision and high efficiency.<sup>5–7</sup> Even though currently being limited by the expensive cost of fabricating process and the occasional unsatisfactory durability performance, successful applications of L-PBF 316L have been seen in specific high value-added scenarios like medical and dental applications, heat exchangers, lightweight structures.<sup>8</sup> Generally, higher porosity is encountered in AM parts due to incomplete fusion, if compared to wrought material. AM 316L SS has yet achieved significant success with near full density and good tensile properties.<sup>9</sup>

Notable progress in manufacturing processes and experimental analysis based on strength parameters have been achieved for AM components. There are recently a flood of publications on L-PBF 316L in terms of many aspects: corrosion,<sup>10–14</sup> fatigue,<sup>15–18</sup> microstructure,<sup>19–25</sup>

mechanical strength,<sup>26–30</sup> tribology,<sup>31–33</sup> and so on. On the one hand, existing researches indicate that this material shows a lot of differences compared to the conventionally fabricated ones; on the other hand, efforts are still required to better reveal the properties and performances as they are highly connected to the fabrication process.

Despite sharing the same fusion-solidification process, L-PBF is quite different from casting because fusion-solidification happens at a very small scale. In the L-PBF process, a sequence of melt pools assembles one built layer. The repetitive layer-by-layer building process yields a very fine microstructure. The laser beam that is the input energy source fast sweeps over the thin layer of powders on the built part, creating a special thermal environment. The microstructure of as-built L-PBF materials is thus distinct from conventional ones. The unique microstructure of L-PBF 316L has a notable impact on mechanical behavior. The refined grains have a Hall–Petch strengthening mechanism. The grain morphology is not as equiaxed as the conventional one. The non-isotropic crystallographic orientations bring anisotropy to the mechanical responses. Due to the high dislocation density at the grain boundaries resulting from a high cooling rate, the L-PBF 316L shows a good yield strength without losing ductility.<sup>34</sup> Further exploration of the cellular dendrite of as-built L-PBF 316L indicates that the dissociation of tangled dislocation on the cell wall provides the barriers to plastic deformation.<sup>35</sup> These substructure colonies accommodate strain localization offering resistance to slip transmission of inhomogeneous microstructures.<sup>36</sup>

The material's constitutive behavior is strongly connected to its microstructure. Characteristic AM-origin microstructures in L-PBF 316L can be enumerated: melt-pool boundaries, cellular walls, precipitates, impurities, elemental segregations, local lattice misorientations, and so on.<sup>37</sup> Elongated grains, often seen in the additive manufactured 316L due to the epitaxial growth following the thermal gradient direction, have negligible influence on the macroscopic yield behavior.<sup>38</sup> Numerous investigations concerning the high cycle fatigue (HCF) behavior of L-PBF 316L have attributed the dominant source of fatigue failure to the inherent defect,<sup>39–42</sup> while the role of AM microstructure has been less discussed. The evolution of texture and porosity was characterized during uniaxial tensile loading of 316L using in situ  $\mu$ -CT and high energy X-ray diffraction in the work of Leonard et al.<sup>43</sup> This study shows that elastic strains accumulate more in the grains oriented in {200} direction and less in the grains oriented

in the {111} and {220} directions under monotonic tensile loading. This behavior is in line with knowing that the deformation of 316L is dominated by crystallographic slip on the {111}<110> system. However, very few researches shed light on the evolution of AM microstructure of 316L with cycling.

Under cyclic loading, a notable phenomenon is the hardening and softening since the microstructure undergoes a series of changes. Zhou et al.<sup>44</sup> performed low cycle fatigue (LCF) tests on the wrought 316L with a number of samples being surface-treated to improve the compressive residual stress. It is seen that the wrought 316L with or without surface treatment shows a long-term softening, which follows the initial hardening occurring during the first several cycles, as shown in Figure 1A. In the work of Mazánová et al.,<sup>45</sup> it is reported that the cold worked 316L shows cyclic softening followed by long-term cyclic hardening under room temperature cyclic straining as depicted in Figure 1B. For cold worked 316L, the initial cyclic softening is due to the formation of low energy dislocation structures and the secondary cyclic hardening is due to the gradual formation of deformation-induced  $\alpha'$ -martensite. Cold work can improve the yield strength of material by introducing high dislocation density inhibiting the slip. L-PBF has a similar strengthening mechanism. Yu et al. performed LCF tests for the L-PBF 316L.<sup>46</sup> A continuous softening occurs because the dislocations undergo unpinning from the cell boundaries and planar movement, as shown in Figure 1C.

Besides the characteristic microstructure, L-PBF materials in the as-built state also present noticeable surface roughness as well as defects. Indeed, these defects can be eliminated (or reduced) and the microstructure can be altered by post-treatments.<sup>34</sup> To improve mechanical performance, post-treatments are still essential to AM products but diminish the charm of AM at the same time. Post-manufacturing processes, such as machining and polishing, may not always be feasible for AM parts, for instance, in hollow-shaped products. For that reason, knowing the performance of parts containing defects is essential. Literature reported that the tensile elongation-to-failure of L-PBF 316L is sensitive to the built-in flaws.<sup>37</sup> But the tested samples in that reference were very small in dimension (length <3 mm). Thus, the built-in flaws were relatively significant and played an important role. For samples with inherent roughness, the role of surface imperfections in the ductility and the cyclic mechanical behavior is still worthy of being explored.

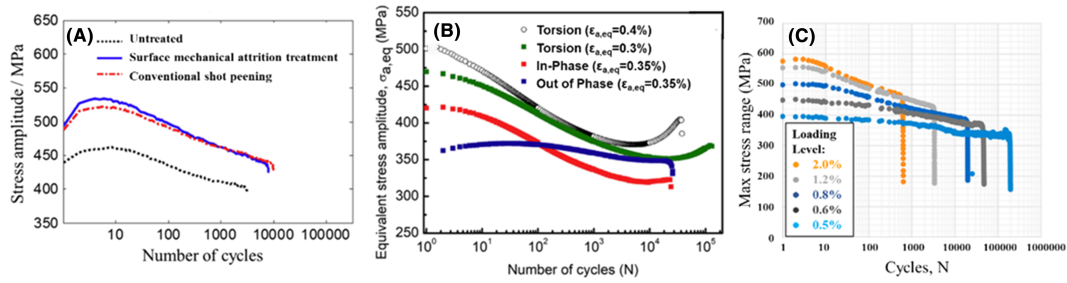


**FIGURE 1** Cyclic hardening/softening curves of (A) different surface-treated samples under  $\Delta\epsilon/2 = \pm 0.5\%$  (wrought 316L),<sup>44</sup> (B) samples loaded with various strain paths (cold worked 316L),<sup>45</sup> (C) samples under different loading levels (selective laser melting (SLM) 316L)<sup>46</sup> [Colour figure can be viewed at [wileyonlinelibrary.com](http://wileyonlinelibrary.com)]

In this work, we perform a series of experimental investigations on the microstructures of as-built L-PBF 316L before and after cyclic loadings. Both strain-controlled and stress-controlled cyclic loadings are tested. The aim is to better understand the roles of L-PBF characteristic microstructural features in the cyclic mechanical behavior. As the HCF is expected to be very sensitive to the surface state, half of the as-built HCF specimens have been polished to provide more references in the condition that the defects are not exaggerated. The microstructures of the as-built samples and the tested samples are examined to explore the role of microstructure in LCF and HCF regimes.

## 2 | MATERIAL AND METHODS

### 2.1 | Powder characterization

An austenitic SS 316L powder (supplied by the Weare Group) is used for the manufacturing process. This batch of powder is recycled. The oxygen rate is less than 1000 ppm, and the powder is considered appropriate for providing quality AM parts. Comprehensive characterizations are thus conducted to assess the powder's characteristics:

- The analysis of the chemical composition of the studied 316L powder confirmed that composition is close to the nominal (normalized) one.
- Laser granulometry analysis is realized on two powder samples (samples A and B with distributions displayed on Figure 2A) to check the repeatability. The particle size is described by  $D_{10}-D_{90}$  (where  $D_{xx}$  is the equivalent volumetric diameter at the cumulative probability

of  $xx\%$ ). The particle size in the delivery state is 5–25  $\mu\text{m}$ .

- From the microscopic observations shown in Figure 2B, the particles appear to be predominantly spherical but sometimes show asymmetrical satellite-like shapes. The satellite-like particle is formed when small particles stick to a larger one during solidification in the previous fabrication process. Powder recycling can lead to oxidized particles which are a source of internal imperfection.
- The microstructure of a powder particle can be observed after the chemical attack. The scanning electron microscope (SEM) observation (see Figure 2C,D) shows the powder is almost a single phase and has a fine microstructure with an average grain size of fewer than 4  $\mu\text{m}$ .

### 2.2 | Specimens preparation

The L-PBF machine ProX DMP 320 was used with the optimal process parameters for 316L SS (listed in Table 1). Two identical jobs were conducted. On each build plate, there were 15 cylindrical specimens with different diameters for microstructure and internal defect characterization tests, 5 tensile specimens for monotonic and cyclic mechanical tests, and 15 fatigue specimens.

A stress-relieving treatment was carried out on the assembly before the separation of the specimens from the tray. This treatment, which is similar with that used in the literature,<sup>47</sup> aims at mitigating the residual stresses without modifying the as-built microstructure of 316L SS. It should be mentioned that a procedure with a holding temperature of 900°C for 2 h followed by water

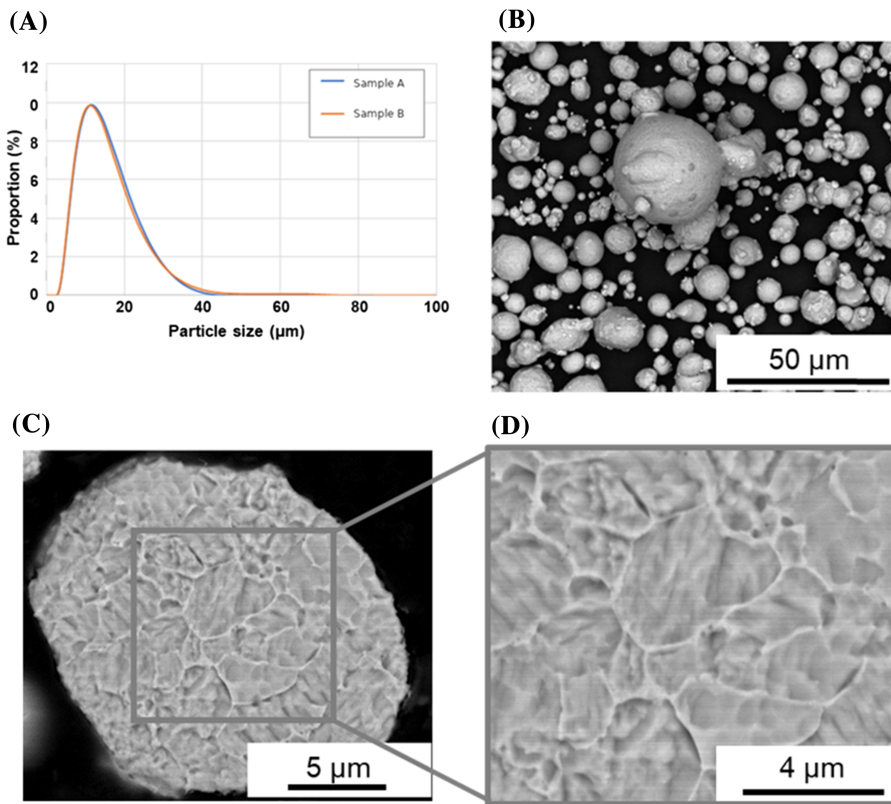


**FIGURE 2** Characterization of powder 316L steel: (A) distribution of powder size, (B) shapes of powder particles, and (C, D) microstructure of powder [Colour figure can be viewed at [wileyonlinelibrary.com](http://wileyonlinelibrary.com)]

**TABLE 1** Processing parameters for L-PBF 316L SS

Machine	Process parameters					Scanning strategy
<b>ProX DMP 320</b>	Laser spot size	Scanning speed	Power	Hatch spacing	Layer thickness	Random island <b>without contouring strategy</b>
	0.07 mm	700 mm/s	275 W	0.07 mm	30 μm	

quenching is recommended by ASM 2759 to eliminate the residual stress. However, such a heat treatment will change the microstructure. The used heat treatment consists of a holding at a temperature of 620°C for 90 min followed by a natural cooling for 800 min until the temperature drops to 180°C. This treatment is conducted in the air atmosphere without environmental control. X-ray diffraction has been performed to measure the residual stress on the surface. The heat treatment did not completely relieve but mitigate the residual stresses, which is in accordance with the results of Riemer et al.<sup>47</sup> The measured residual stress was in a range of 100–200 MPa, existing as tensile stress. The shear stress component was almost zero.

Additionally, profilometry characterization has been performed on the as-built specimens. Measurements at different sites indicated that the average roughness is 15 μm (Ra). In the HCF tests, half of the samples have been surface-treated using different grit sandpapers to

achieve an average surface roughness, Ra, of less than 1 μm.

Finally, X-ray μCT tomography revealed the fabricated specimens have good density without large pores inside. The porosity rate is under 0.1%

### 2.3 | Mechanical testing

All the mechanical tests are conducted in ambient air and temperature on a biaxial servo-hydraulic testing system, MTS® 809. First, monotonic tensile tests are performed with two surface state samples: the as-built surface state and the polished surface state sample. Each sample was subjected to monotonous tension until it broke. Then, another series of tests was conducted to characterize the cyclic mechanical behavior of 316L steel using the same machine. On the one hand, the strain-controlled tests were carried out on the as-built

specimens with a loading ratio of  $R = -1$  and a strain rate of  $10^{-3} \text{ s}^{-1}$ . On the other hand, the stress-controlled tests were carried out on the as-built and polished specimens with a loading ratio of  $R = -1$  and a loading frequency of 15 Hz. Temperatures were measured by a thermocouple during the tests. No evident self-heating was observed.

## 2.4 | Microstructure characterization

Optical microscope (OM), SEM, and electron backscatter diffraction (EBSD) are used to characterize the microstructure both before and after the mechanical tests.

## 3 | RESULTS

### 3.1 | Macrostructure and microstructure of L-PBF 316L SS

The observations were carried out on two planes: (i) the Z-plane, also called manufacturing or lasing plane, is the plane perpendicular to the building direction Z, it contains the history of a single layer; and (ii) the X/Y plane, it is the plane perpendicular to X or Y axis and parallel to

the Z axis. This plane is constructed layer by layer and therefore contains the thermal history of all layers.

The microscopic structure of the Z plane can be seen in Figure 3A–C. It is possible to distinguish melting beads corresponding to the main direction of the laser displacement. On this plane, the section of the austenitic grains is quadrangular. The laser path is visible when changing directions. With respect to the X/Y planes (see Figure 3D–F), we can see ellipses, characteristic of the L-PBF process since they represent a section of the melt pools which appear during the passage of the laser. The macrostructure resembles fish scales. The observation of these planes makes it possible to distinguish the interfaces between the layers clearly and to see the elongated shape of austenitic grains crossing several layers. We can also observe the grains that are formed during the manufacturing process. Their growth direction roughly coincides with the Z-axis of the specimen. As depicted in Figure 3B,C, the thermal-origin alignment of austenitic grains indicates the epitaxial growth of grains, that is, the grains tend to grow along the building direction. From the lateral plane observations (Figure 3E,F), the columnar grains are oriented along the Z axis and pass through several layers. Conventionally, the preferred direction of growth in face center cubic (FCC) materials is the  $\langle 001 \rangle$  direction. In L-PBF, despite the high cooling rates ( $\approx 10^6$

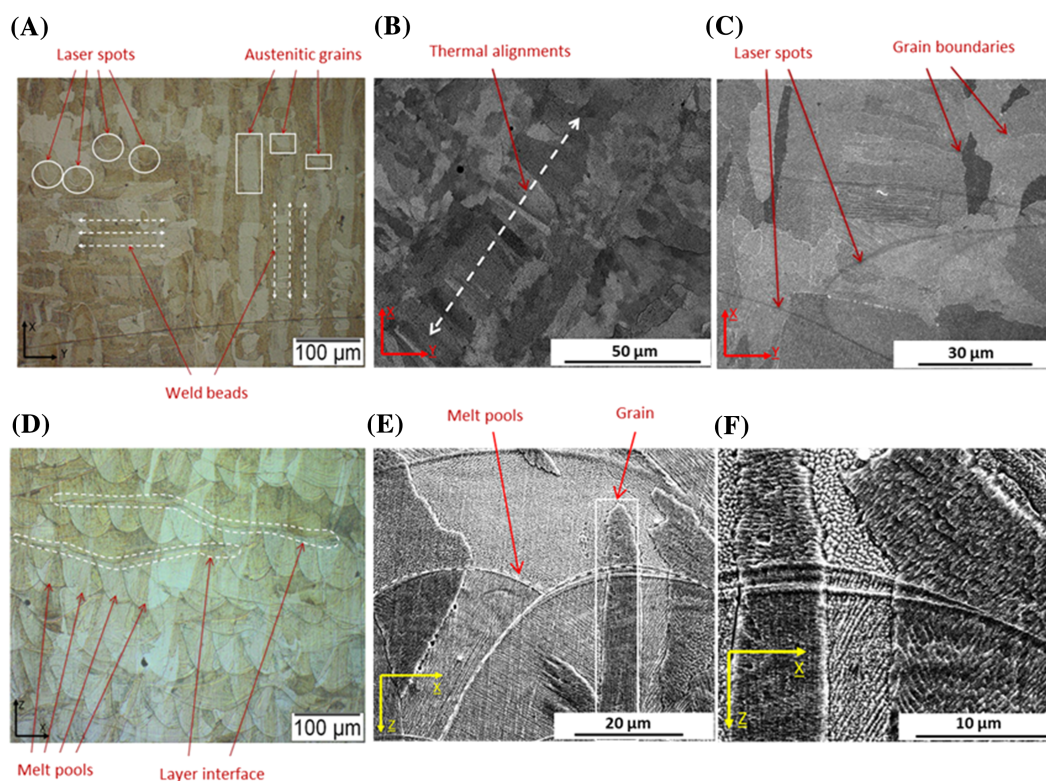


FIGURE 3 Macrostructure and microstructure observed on (A–C) a lasing plane Z and (D–F) a lateral plane X/Y [Colour figure can be viewed at [wileyonlinelibrary.com](http://wileyonlinelibrary.com)]

K/s), this preferred direction of growth is respected. Most grains grow along the direction perpendicular to the solidification front formed by the melt pools. The grains are columnar, pass through the melt pools, and consist of dendrites resulting from rapid solidification after the laser passage.

To get a better knowledge of the microstructure, EBSD was used to analyze the grain morphology and orientation. Post-treatment of the EBSD results was performed using the ATEX software.<sup>48</sup> This post-treatment leads to EBSD mapping (with reconstituted grains) shown in Figure 4. The grain size is not homogeneous in the observed samples. Elongated columnar grains that cross several layers are visible, and there are no twinning boundaries in these maps. This texture has been widely observed in the literature regarding the L-PBF process. Other grain morphologies and textures have also been observed by modifying the process parameters. The volumetric energy density, defined as being the ratio between the laser power and the product of the laser scanning speed, the hatch spacing and the layer thickness, modifies both the melt pool shape and the crystallographic grain growth. Choo et al.<sup>49</sup> studied the effect of laser power on the texture formed during the manufacture of 316L cylinders by L-PBF. In this study the laser power varies from 380 to 200 W while keeping the other parameters constant ( $v = 300$  mm/s, diameter = 0.207 mm, layer thickness = 60  $\mu\text{m}$ , hatch spacing = 100  $\mu\text{m}$ ). A 90° rotation of the pattern (zig-zag) is performed between each layer. Changing the power while keeping the other parameters constant is the same as changing the energy density provided by the laser. At high power (380 W), a strong texture (100) is observed along Z.<sup>49</sup> It corresponds to the direction of preferential solidification of FCC materials. At an intermediate power (260 W), the texture (110) is predominant. Finally, at low power (200 W), the overall orientation of the grains is random.

This change in texture is hence a function of power and the shape of the melt pools plays an important role.

As a matter of fact, whatever the power, the grains (001) grow according to the thermal gradient, and therefore radially in the melt. At 380 W, the melt pools are flat and wide, the grains grow vertically. For intermediate power values, the melt pools are less flat. The radial growth of the grains (001) associated with the covering of the weld beads, therefore, generates an overall texture (110) along with Z. This is the principle of the chevron growth between weld beads explained by Andreau et al.<sup>50</sup> Finally, at low power, the melt pools remain round but no longer overlap enough to generate epitaxial growth, so the texture is more isotropic. Sun et al.<sup>51</sup> studied a higher power domain. They find that, at very high power, the melt pools are very deep and fine while at medium power the melt pools are less deep and wider. This results in differences in the shape of the solidification front, which directly impacts the direction of grain growth. At very high power, the pool is in a keyhole regime, so it is excessively deep and thin at its end. This particular form allows the growth of the planes  $\langle 110 \rangle // Z$ . For medium powers, the shape of the solidification front allows the epitaxial growth of grains  $\langle 001 \rangle // Z$  from the bottom of the melt.

The preferential orientation of the grains has a significant impact on their elastoplastic behavior. It has been shown that grains oriented  $\langle 001 \rangle // Z$  deform by plastic sliding while those oriented according to  $\langle 110 \rangle // Z$  essentially deform by micro/nano-twinning. This results in a much better ductility and resistance of the materials with the orientation  $\langle 110 \rangle // Z$  predominant (TWIP effect). Several lamellar crystallographic composites are studied to combine the beneficial effects of each of the orientations.<sup>51</sup> This kind of microstructure was also obtained by Andreau et al.<sup>50</sup>

### 3.2 | Monotonic tensile behavior

The stress-strain curves of as-built and total-polished specimens are plotted in Figure 5. Due to the

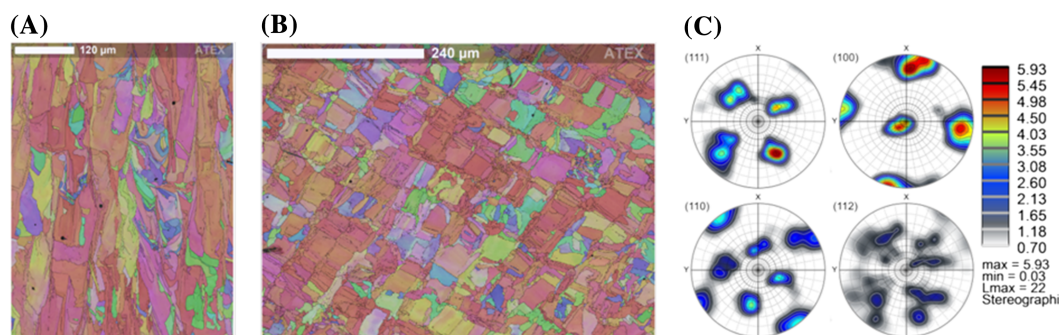
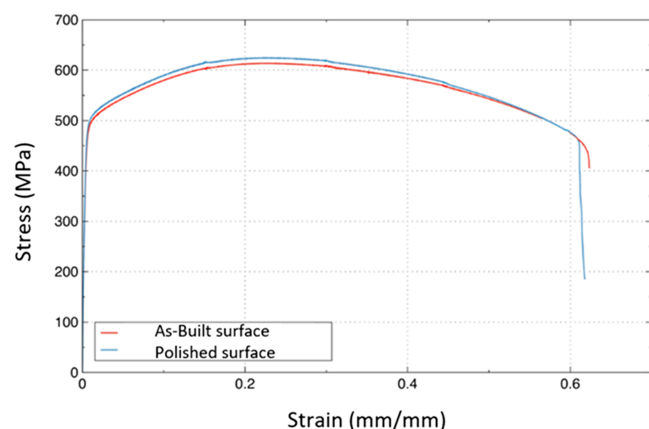


FIGURE 4 Electron backscatter diffraction (EBSD) maps of (A) lasing plane Z and (B) lateral plane X/Y. (C) computed pole figures [Colour figure can be viewed at wileyonlinelibrary.com]

extensometer's range limitation, the extensometer was reset to zero once the measured strain reached 15%. The reinitiating of the extensometer was repeated 4 times to reach an elongation of the specimen at about 60%.

As shown in Table 2, gathering data from the literature, a large range of mechanical properties is found and can be attributed to the variety of the manufacturing parameters used. Note that only data from manufactured vertically components are collected (except for ASM Handbook, which is the reference value for wrought 316L). Compared to that obtained conventionally, the significant increase (35%–100%) in the Yield Strength (YS) of 316L steel obtained by L-PBF could be explained by the multiscale structuring of the microstructure, in particular the presence of cellular dislocation substructures. The latter would induce hardening of the material



**FIGURE 5** (A) Tension curves for the as-built surface specimen (red) and for the polished surface specimen (blue) and (B) the corresponding fitting Young Modulus from polished specimens [Colour figure can be viewed at [wileyonlinelibrary.com](http://wileyonlinelibrary.com)]

by the Hall–Petch effect, according to certain authors.<sup>52</sup> Recently, this hypothesis is verified by Bahl et al.<sup>20</sup> as well as by Li et al.<sup>37</sup> The latter report respectively that the relation of Hall Petch cannot be applied in such a simple way.

The Ultimate Tensile Strength (UTS) remains in the same order of magnitude (but often in the upper range) but it is known that the defects are more numerous in the materials obtained by L-PBF (in particular porosities).

The special feature of L-PBF 316L is its high YS/UTS ratio (Table 2). It is generally between 0.7 and 0.9 for the studied material, whereas it is conventionally between 0.4 and 0.5. This is all the more interesting since, for conventional materials, an increase in this ratio generally leads to a reduction in the elongation at break. However, for the 316L steel obtained by L-PBF, the strain to failure remains generally the same or is even better. This high value of YS/UTS ratio is probably associated with the hardening induced by the L-PBF process. During fabrication, due to the high thermal gradients, constraints arise at the grain scale, which implies the creation of numerous dislocations, themselves being at the origin of the work hardening.

### 3.3 | Cyclic tension-compression behavior

Because the L-PBF 316L may have the characteristics of cyclic softening, it is difficult to determine the moment of failure via setting the load threshold of the machine. In this experiment, analysis was performed after the loading was completed to determine the number of failed cycles. The hysteresis curves and softening curves were obtained so as to determine the moment of failure. There were two

**TABLE 2** Manufacturer and literature data of the mechanical properties in uniaxial tension of 316L SS obtained by L-PBF

	UTS (MPa)	YS (MPa)	YS/UTS	A%	E (GPa)
<b>Releasing Heat-treated—Present study</b>	<b>610–630</b>	<b>450–470</b>	<b>0.74</b>	<b>60</b>	<b>150–157</b>
As built—manufacturers data EOS <sup>53</sup>	540 ± 55	470 ± 90	0.87	50 ± 20	180
As built—SLM Solutions <sup>53</sup>	654 ± 49	550 ± 39	0.84	35 ± 4	169 ± 31
As built—Tolosa 2010 <sup>54</sup>	570–590	530–560	0.94	42–45	
As built—Kuznetsov 2016 <sup>55</sup>	685–708	567–582	0.83	34–35	
As built—Liverani 2017 <sup>56</sup>	540–570	420–500	0.84	40–70	
As built—Riemer 2014 <sup>47</sup>	565	462	0.82	54	
As built—Bahl 2019 <sup>20</sup>	565 ± 10	480 ± 20	0.85	44 ± 5	
As built—Spierings 2011 <sup>17</sup>	760	640	0.84	30	
As built—Salman 2019 <sup>27</sup>	1016 ± 8	550 ± 10	0.54	50	
<i>Forged, ASM Handbook (1993)</i>	620	310	0.5	30	205

criteria for determining the moment, and both were based on softening by a number of cycles. First, the sample is considered broken if the tangent to the softening curve begins to rotate clockwise and the change in inclination is greater than  $1^\circ$  for every 10 cycles. The value was found empirically. The second criterion is based on the maximum stress drop. Failure is noted as the drop begins to exceed 0.5 MPa at the 10-cycle interval. The values obtained for the two criteria are close. Their average was used as the final value corresponding to the break. Table 3 characterizes the imposed strain levels, the number of cycles before failure, and the stress amplitude at the half-life cycle (Table 3).

In Figure 6, the asymmetry of softening phenomenon in the tension and the compression directions is noteworthy. For all four different loading levels, the maximum compression stress in each sample quickly decreases during the first quarter of the fatigue life and tends to be stabilized in the following loading cycles while the

maximum tensile stress in each sample decreases steadily throughout the load cycle except for the sample that was subjected to the loading of  $\Delta\varepsilon = \pm 0.30\%$ . One possible explanation is that the samples have remaining residual stress in the compression direction. The softening of the material during the tests can be observed on the softening curves, plotted for each level of deformation, and compared in Figure 7. In LCF, it is not unusual to observe a cyclic softening. This behavior is also seen on wrought 316L steel.<sup>57,58</sup> Regarding the wrought 316L, the softening trend is evident even if the tension-compression loading level is only at about  $\pm 0.18\%$  (see Figure 7). But for the L-PBF 316L, at a loading level of  $\pm 0.30\%$ , the cyclic mechanical responses are relatively constant. Softening is pronounced at higher loading levels, such as  $\pm 0.45\%$ . Note that the compared wrought 316L has been surface treated while the L-PBF 316L has been tested in the as-built state. But the L-PBF 316L undergoes more than 1000 cycles at the loading level of  $\pm 0.45\%$ . Meanwhile,

Sample name	Strain (%)	Rupture (cycles)	$\Delta\sigma/2$ at half-life (MPa)
Tray 2, sample 5	$\pm 0.30$	81,815	303
Tray 1, sample 1	$\pm 0.45$	10,931	362
Tray 2, sample 2	$\pm 0.60$	5390	377
Tray 1, sample 4	$\pm 0.75$	2767	398

TABLE 3 Low cycle tension-compression fatigue tests

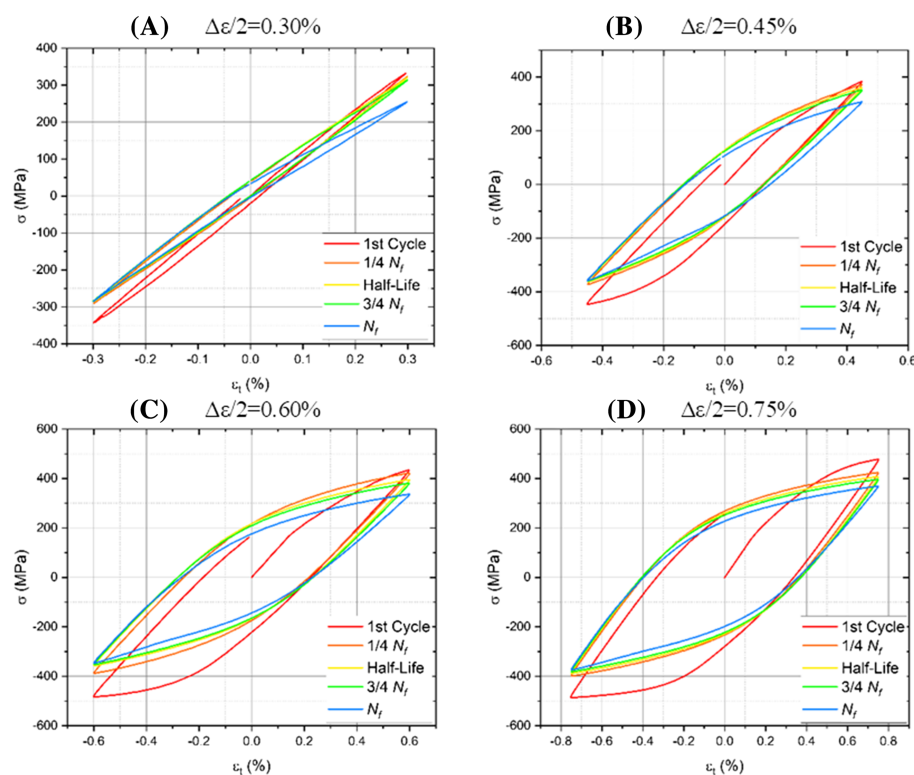


FIGURE 6 Hysteresis loops at the selected cycles of samples subjected to loading of  $\Delta\varepsilon = 0.3\%$ ,  $0.45\%$ ,  $0.6\%$ , and  $0.75\%$  [Colour figure can be viewed at [wileyonlinelibrary.com](http://wileyonlinelibrary.com)]

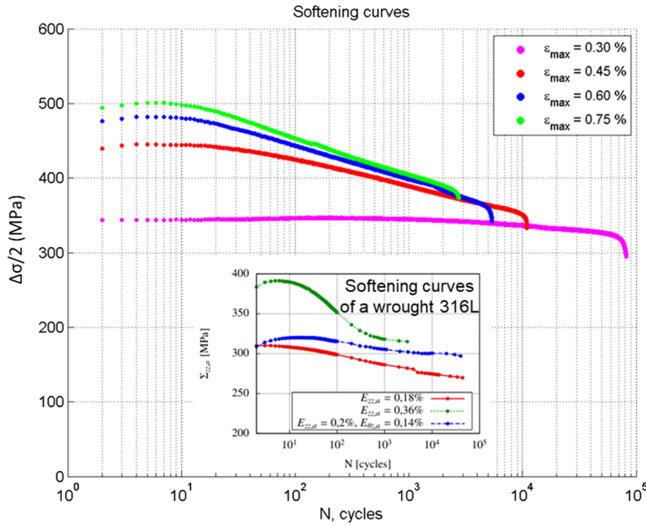


FIGURE 7 Cyclic softening curves under different cyclic deformations as well as reference for a wrought 316L<sup>51</sup> [Colour figure can be viewed at wileyonlinelibrary.com]

the wrought 316L failed before 1000 cycles at the loading level of  $\pm 0.36\%$ .

The correlation between the elastic strain and the fatigue life can be characterized by the Basquin relationship shown in Equation (1), in which  $\Delta\epsilon_e$  denotes the elastic strain range,  $\sigma'_f$  is the fatigue strength coefficient,  $E$  denotes Young's modulus,  $N_f$  is the number of cycles to failure, and  $b$  is the fatigue strength exponent.

$$\frac{\Delta\epsilon_e}{2} = \left(\frac{\sigma'_f}{E}\right) (2N_f)^b \quad (1)$$

And, the correlation between the plastic strain range and the fatigue life can be characterized by the Coffin-Manson relationship Equation (2), in which  $\Delta\epsilon_p$  denotes the plastic strain,  $\epsilon'_f$  is the fatigue ductility coefficient, and  $c$  is the fatigue ductility exponent.

$$\frac{\Delta\epsilon_p}{2} = \epsilon'_f (2N_f)^c \quad (2)$$

Thus, the relation between total strain range and fatigue life can be expressed as a formula shown in Equation (3), in which  $\Delta\epsilon_t$  denotes the total strain range.

$$\frac{\Delta\epsilon_t}{2} = \left(\frac{\sigma'_f}{E}\right) (2N_f)^b + \epsilon'_f (2N_f)^c \quad (3)$$

The strain-life curves are plotted in Figure 8 in the double-logarithmic coordinate. The fatigue life is

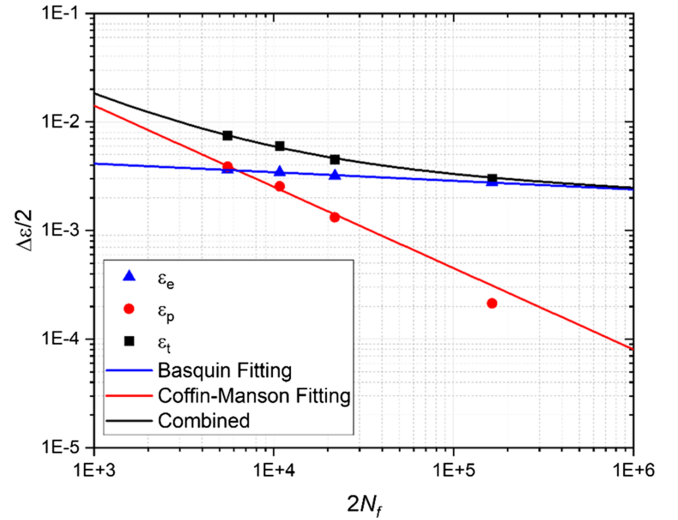


FIGURE 8 Strain-life plots of low cycle fatigue (LCF) tests of selective laser melting (SLM) 316L with fitted curves [Colour figure can be viewed at wileyonlinelibrary.com]

expressed by the number of load reversals, that is,  $2N_f$ . The fitted expressions are respectively as follows:

$$\begin{aligned} \frac{\Delta\epsilon_e}{2} &= 0.7138 * (2N_f)^{-0.079} \\ \frac{\Delta\epsilon_p}{2} &= 2.4955 * (2N_f)^{-0.748} \end{aligned} \quad (4)$$

$$\frac{\Delta\epsilon_t}{2} = 0.7138 * (2N_f)^{-0.079} + 2.4955 * (2N_f)^{-0.748}$$

### 3.4 | HCF behavior

Fatigue limits are determined by the staircase method. The as-built specimens have a fatigue limit of 93 MPa (run-out at  $2*10^6$  cycles), and the polished specimens have a fatigue limit of 115 MPa. By removing the surface roughness, an increase of 24% in fatigue limit is obtained for the L-PBF 316L products. Hence, the surface treatment is effective in terms of endurance improvement. It is noteworthy that the fatigue limit of the tested L-PBF samples is significantly worse than that ( $\sim 250$  MPa) of the conventionally fabricated counterpart. Nevertheless, similar results are also seen in the literature<sup>41,59</sup> for the as-built surface without contouring strategy.

S-N curves are plotted in Figure 9. In the finite fatigue life stage, both the as-built and the polished samples have the visible trend that fatigue life increases as the loading level decreases. The slopes of the increasing fatigue life of the two groups are close to each other. The polished

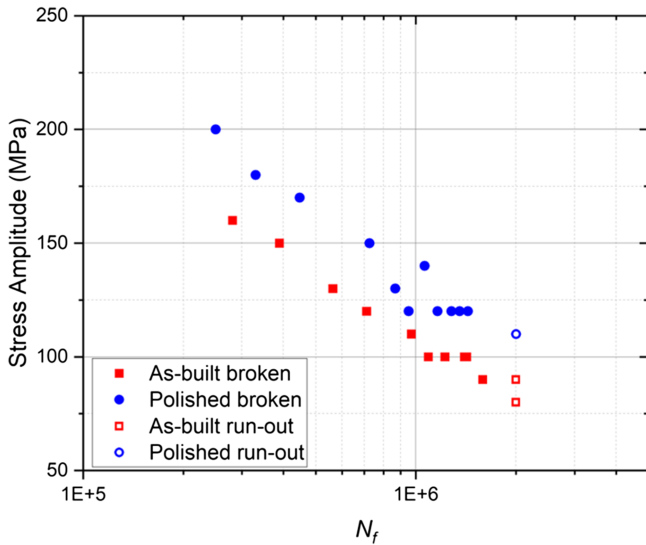


**FIGURE 9** S-N plots of selective laser melting (SLM) SS 316L at a loading ratio  $R = -1$ . Red markers denote the surface-treated samples and blue markers denote the as-built samples. Run-out threshold is set  $2 \cdot 10^6$  cycles [Colour figure can be viewed at [wileyonlinelibrary.com](http://wileyonlinelibrary.com)]

samples always show better fatigue performances compared to the as-built samples.

## 4 | DISCUSSIONS

### 4.1 | Young's modulus of 316L obtained by L-PBF

The Young's modulus of 316L obtained by L-PBF is generally lower than the one of wrought 316L. Several explanations exist in the literature. Some authors link this drop to the crystalline anisotropy of the material.<sup>60,61</sup> Simulations are conducted to verify this assumption.

It is found that the studied material is in a strongly textured state, while the monotonic tensile test reveals that Young's modulus is apparently lower than the nominal value of steel. A self-consistent method<sup>62</sup> is used to mimic the tensile test to predict the elastic behavior. Young's modulus is deduced by using the macroscopic stress divided by the macroscopic strain in the loading direction.

In this simulation framework, the microstructure attributes are taken into account, containing the grain size and the crystallographic orientation. From the EBSD analysis, we can collect the actual size and orientation of each detected grain. These data are imported to the self-consistent model. Raw data from the upper, middle, and bottom areas in the tested specimen are processed

separately to check the results' consistency from different positions and are concatenated together to have an overall estimation of Young's modulus. For comparison purposes, a virtual model with no preferential texture, that is, the crystallographic orientations are distributed randomly, is also calculated. Young's modulus and Poisson ratio are calculated for the isotropically distributed orientations set in the same way as the realistic configuration.

To characterize the anisotropic behavior, the cubic elastic constitutive model is adopted. In light of the absence of elastic constants for L-PBF 316L, the used parameters listed in Table 4 are the ones of  $\gamma$ -Fe<sup>63</sup> because the material is almost purely austenitic. This material has a strong anisotropy with an anisotropic factor of 3.64.

The calculated Young's moduli are listed in Table 5. From the table, we can see that the estimations reached from different simulations are similar. The upper part has the lowest value, and the bottom part has the highest value. The value from the middle part is approximately the same as the value from the concatenated model. However, the simulated moduli have a difference of about 10% with the experimental measurement. A possible explanation is that we have no available exact cubic elasticity model parameters. The parameters from  $\gamma$ -Fe seem to provide good approximations even though a specific deviation exists.

To conclude, the 316L steel produced for this study has mechanical tensile properties comparable to the literature. A slight increase in strain to failure is observed (60% against a maximum of 54% in the literature).

### 4.2 | Comparison between LCF and HCF behaviors

In the LCF tests, the stress amplitude of each sample at half of the fatigue life was extracted. These data combined with the results in HCF tests were plotted as a Wöhler diagram shown in Figure 10. The relation between the stress amplitude and the fatigue life was fitted using the Basquin relationship for the LCF results and HCF results separately. It can be seen that the slopes of the two fitted lines are different. If extrapolation was performed by using the curve fitted by the LCF test data to predict the fatigue life of the material under lower load, the actual fatigue performances of the HCF samples were much worse than those of the prediction. This difference indicated that the fatigue mechanism might be different under different loading levels. To have a better understanding of the cyclic mechanical behavior, the microstructures of the tested samples were comprehensively observed.

TABLE 4 Parameters of cubic elastic constitutive models

C1111 (GPa)	C1122 (GPa)	C1212 (GPa)	Anisotropic factor $2^*C1212/(C1111-C1122)$
197	125	122	3.64

TABLE 5 Computed Young's moduli and Poisson ratios for different sampling areas of EBSD specimen

	Middle	Upper	Bottom	Overall	Experiment	Isotropically distributed	316L Nominal
Number of orientations	2143	4500	3096	9739	—	9000	—
Young's modulus [GPa]	145.1	140.9	146.6	144.6	150–157	194	190–205
Poisson ratio	0.325	0.312	0.304	0.312	N/A	0.284	0.265–0.275

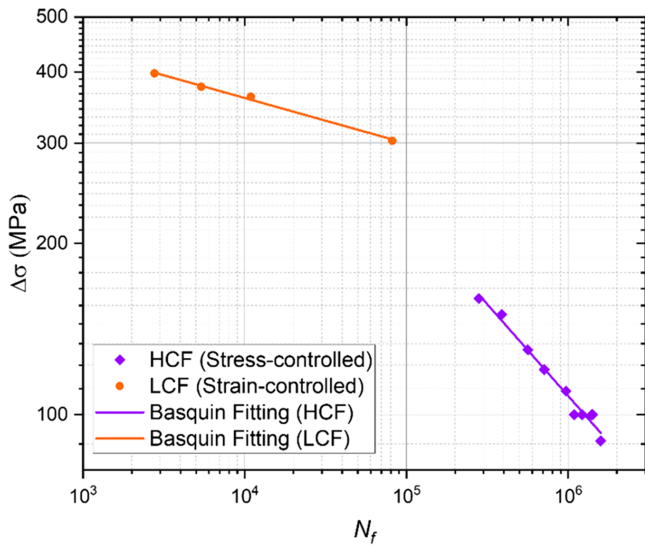


FIGURE 10 Wöhler diagram of the fatigue tests of as-built (without surface treatment) selective laser melting (SLM) 316L samples [Colour figure can be viewed at wileyonlinelibrary.com]

The SEM observations of the LCF microstructure are illustrated in Figure 11. The PSBs are seen pass through the melt pool, which means the melt pool does not bring any strain heterogeneity. Very small cracks formed around the defect (Figure 11A). But the crack did not propagate due to the strengthening mechanism from the sub-grain structure, the cellular dendrite. A zoom view exhibits the structure of the dendritic cell. Precipitates are seen around the cell wall (Figure 11D). These precipitates help the cell walls to block dislocations that enhance the material's strength. Generally, the accumulated plastic deformation leads to the cyclic softening behavior identified during the LCF tests and is responsible for the final failure and the defects have no notable effect on LCF.

In HCF, the SEM observations of the fatigued microstructure are shown in Figure 12A. It can be seen that the cellular dendrites do not present any plastic

deformation and there are no persistent slip bands (PSBs). The melt pool does not have a significant strain concentration either. Both trans-granular and intra-granular fractures can be seen from left to right along the propagation path of the crack.

The HCF performances are dominated by the defect. A typical fractographic observation is shown in Figure 12B. On the fracture surface, it is clearly seen that the fatigue crack initiates at the inherent defects at the subsurface of the specimen. This kind of defect is one of the characteristic defects in the L-PBF process. The unfused powder can be seen inside the defect. It is often called lack-of-fusion (LoF) defect. There are multiple LoF defects at the fatigue initiation site on the fracture surface. The morphology of these defects is worth noting that they exhibit elliptical shapes penetrating the specimen's perimeter. Although there are other LoF defects seen in the core of the sample (not shown in these SEM figures), the internal LoF defects are less seen and have more irregular shapes. Only the LoF defects on or near the surface present such morphological patterns. It can be deduced that the formation of the superficial LoF defects is strongly connected to the precision of the laser path as well as the scanning strategy. To improve the fatigue strength of as-built L-PBF parts, LoF defects should be controlled, in particular on or near the part's surface.

In the LCF regime (shown in Figure 13B), noticeable plastic deformation formed as PSBs inside the large columnar grains. It can be seen that the grains apt to grow along the building direction (denoted red in the orientation maps) exhibit more PSBs compared to the other grains. Besides the effect of grain orientation, it is also found that severe plastic deformation is accumulated at the grain boundaries or around the grains of smaller sizes which is presented as strong misorientation patterns (sometimes shown as black areas due to the insufficient definition precision). In the HCF regime (shown in Figure 13C), the

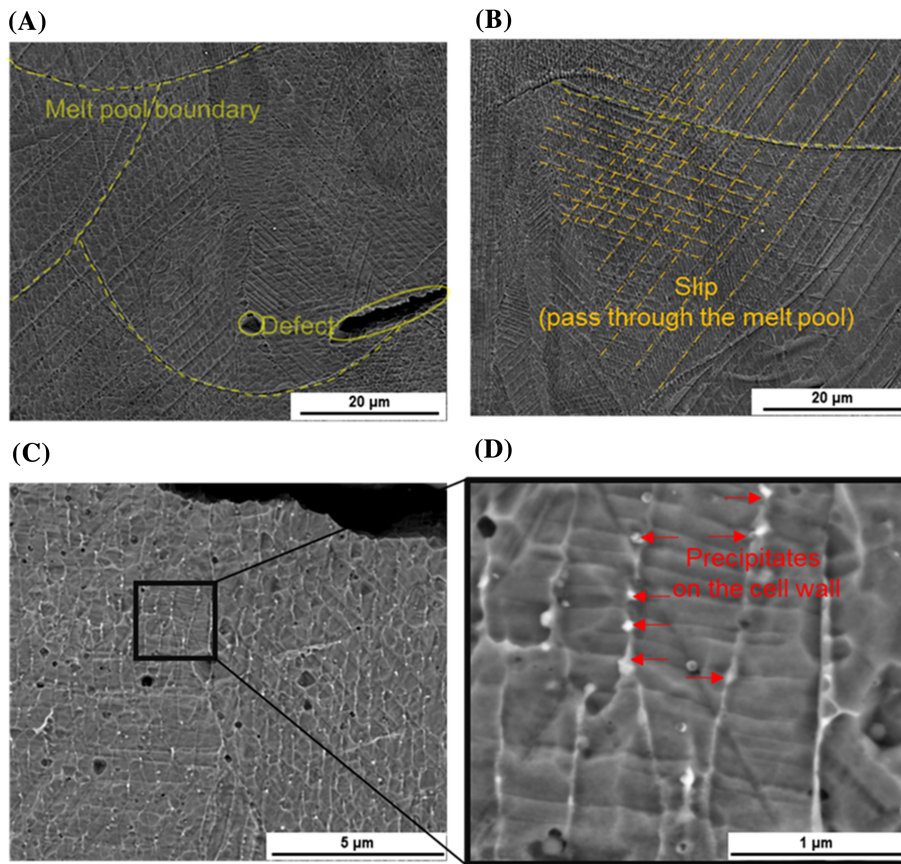


**FIGURE 11** Scanning electron microscope (SEM) observation on the fatigued samples ( $\epsilon = \pm 0.45\%$ , failed at the 10931th cycle): (A) microstructure with presence of defects; (B) slips passing through the melt pool; (C, D) magnified photos of the cellular dendritic network, precipitates can be observed on the cell wall [Colour figure can be viewed at [wileyonlinelibrary.com](http://wileyonlinelibrary.com)]

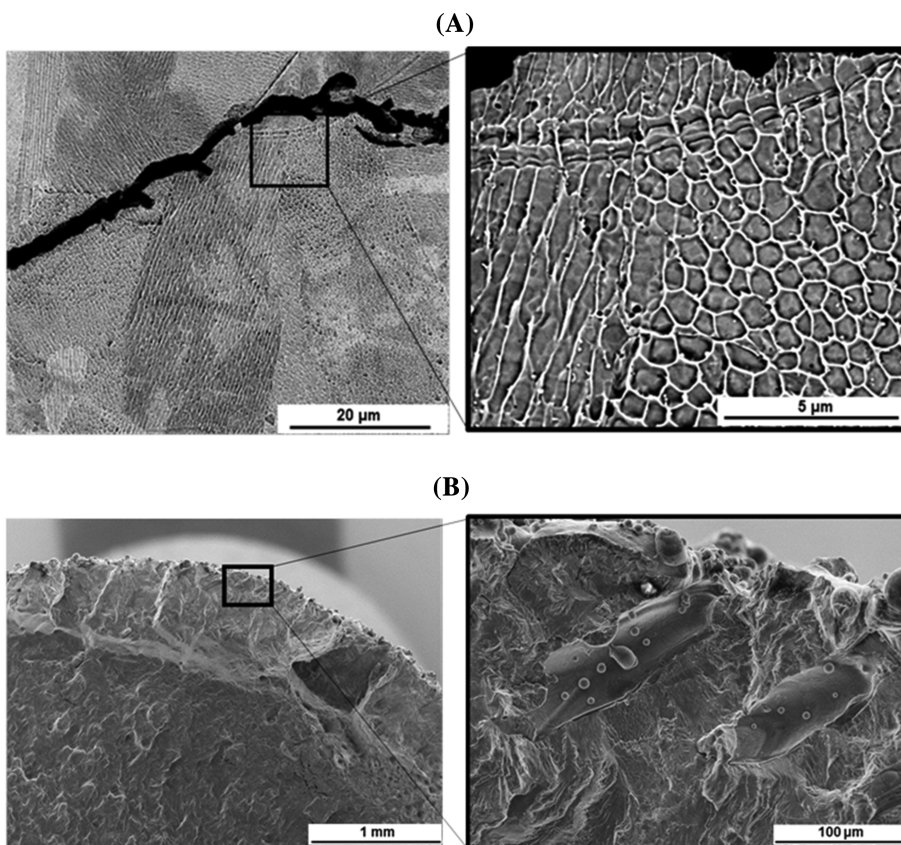


**FIGURE 12** (A) Lateral observations on the crack site, and (B) fractographic observation of a high cycle fatigue (HCF) sample

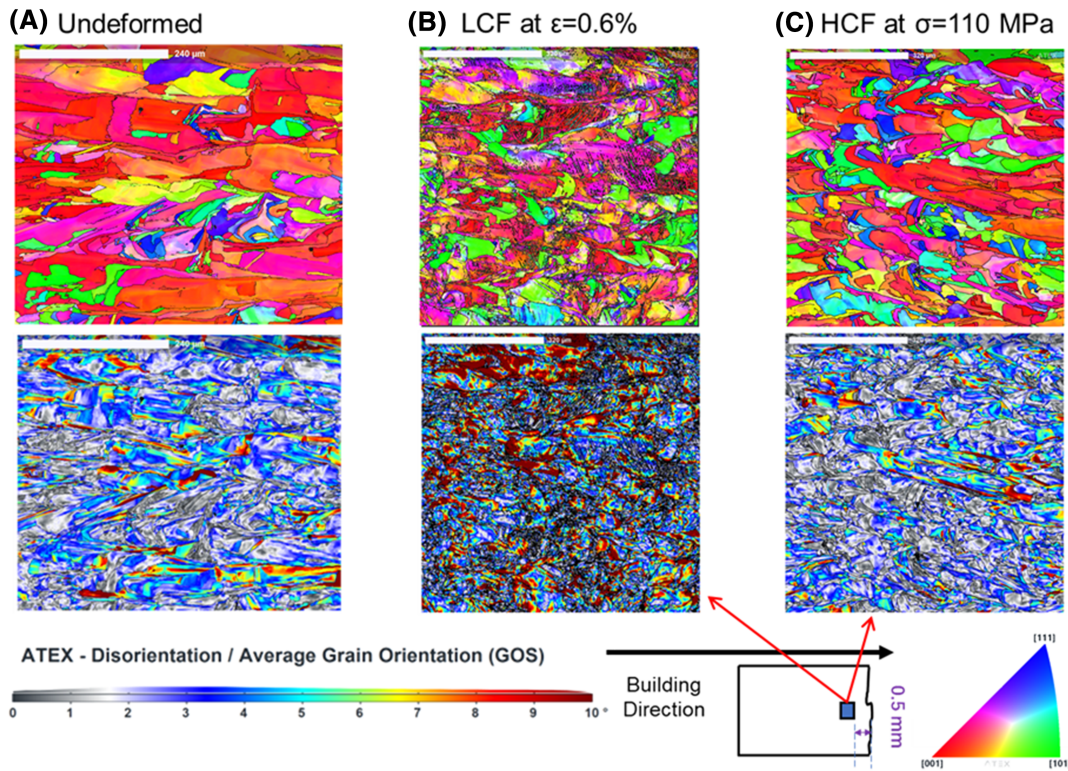


**FIGURE 13** Crystallographic orientation and disorientation mappings of selective laser melting (SLM) 316L stainless steel (SS): (A) undeformed microstructure; (B) after  $\varepsilon = \pm 0.60\%$  cyclic loading and (C) after  $\sigma = \pm 110$  MPa cyclic loading [Colour figure can be viewed at [wileyonlinelibrary.com](http://wileyonlinelibrary.com)]

specimens are subjected to low-level loadings which only generate elastic deformations from the macroscopic vision. Besides, the high fatigue loading applied in this study is far below the macroscopic yield strength. Hence, in the HCF samples, most of the grains remain their original crystallographic orientations. Disorientation is only seen at the grain boundaries. Considering that the applied HCF loading level is very weak in this study (25%–30% of the yield strength), the grains are mostly deformed in the elastic range. Finally, the plastic deformation in HCF is localized around the surface defect.

## 5 | CONCLUSIONS

In this work, investigations on the microstructure and cyclic mechanical behaviors of an L-PBF 316L SS are conducted. The following conclusions can be drawn:

1. Regarding the mechanical behaviors, the characteristic microstructure of L-PBF 316L results in good yield strength and ductility. The anisotropic nature combined with the strong texture causes the low Young's modulus. The monotonic tensile performance of L-

PBF 316L is comparable with that of conventional wrought 316L.

2. The LCF loading generates perceptible plastic deformation mainly exhibited as slip in the samples, while HCF loading does not cause visible plastic deformation indicating the different sources of fatigue crack initiation.
3. The process-driven defects that are LoF defects in the studied material play an essential role in the HCF regime while having a negligible effect in the LCF regime. Besides, by eliminating the surface roughness, the fatigue limit has been notably improved for this material. Preserving the original as-built surface roughness impairs HCF performance while is harmless for LCF performance of L-PBF 316L SS.
4. Microscopic stress heterogeneity is revealed from the PSB exhibition accumulated mostly in the building-direction-oriented grains under LCF loading. By contrast, the microstructure shows no perceptible evolution until HCF failure.

## ACKNOWLEDGEMENTS

The authors would like to thank Nicolas Chambrin, Nikita Dorofeev, and Marco Scarpetta for their time and efforts in conducting the experiments.

## AUTHOR CONTRIBUTIONS

Xiaoyu Liang: Conceptualization, methodology, validation, formal analysis, investigation, writing-original draft, visualization. Anis Hor: Writing-review & editing, methodology, investigation, supervision. Mehdi Salem: Writing-review & editing, investigation. Camille Robert: Writing-review & editing, investigation, supervision. Franck Morel: Writing-review & editing, methodology, formal analysis.

## DATA AVAILABILITY STATEMENT

The data that support the findings of this study are available on request from the corresponding author. The data are not publicly available due to privacy or ethical restrictions.

## NOMENCLATURE

$\Delta\epsilon_e$	elastic strain range
$\Delta\epsilon_p$	plastic strain range
$\Delta\epsilon_t$	total strain range
$\Delta\sigma$	stress range
$\epsilon'_f$	fatigue ductility coefficient
$\sigma'_f$	fatigue strength coefficient
AM	additive manufacturing
$b$	fatigue strength exponent
$c$	fatigue ductility exponent
$E$	Young's modulus
EBSD	electron backscatter diffraction
FCC	face center cubic
HCF	high cycle fatigue
LCF	low cycle fatigue
LoF	lack-of-fusion
L-PBF	Laser Powder Bed Fusion
$N_f$	number of cycles to failure
OM	optical microscope
PSB	persistent slip band
SEM	scanning electron microscope
SLM	selective laser melting
SS	stainless steel
UTS	ultimate tensile strength
YS	yield strength

## ORCID

Xiaoyu Liang  <https://orcid.org/0000-0002-9611-420X>

## REFERENCES

- Herzog D, Seyda V, Wycisk E, Emmelmann C. Additive manufacturing of metals. *Acta Mater.* 2016;117:371-392.
- Frazier WE. Metal additive manufacturing: a review. *J Mater Eng Perform.* 2014;23:1917-1928.
- Ngo TD, Kashani A, Imbalzano G, Nguyen KTQ, Hui D. Additive manufacturing (3D printing): a review of materials, methods, applications and challenges. *Compos Part B.* 2018; 143: 172-196.
- DebRoy T, Wei HL, Zuback JS, et al. Additive manufacturing of metallic components—process, structure and properties. *Prog Mater Sci.* 2018;92:112-224.
- Shamsaei N, Yadollahi A, Bian L, Thompson SM. An overview of Direct Laser Deposition for additive manufacturing; part II: mechanical behavior, process parameter optimization and control. *Addit Manuf.* 2015;8:12-35.
- Olakanmi EO, Cochrane RF, Dalgarno KW. A review on selective laser sintering/melting (SLS/SLM) of aluminium alloy powders: processing, microstructure, and properties. *Prog Mater Sci.* 2015;74:401-477.
- Zhang B, Li Y, Bai Q. Defect formation mechanisms in selective laser melting: a review. *Chinese J Mech Eng English Ed.* 2017;30:515-527.
- Yap CY, Chua CK, Dong ZL, et al. Review of selective laser melting: materials and applications. *Appl. Phys Rev.* 2015;2:041101.
- Lou X, Song M, Emigh PW, Othon MA, Andresen PL. On the stress corrosion crack growth behaviour in high temperature water of 316L stainless steel made by laser powder bed fusion additive manufacturing. *Corros Sci.* 2017;128:140-153.
- Al-Mamun NS, Mairaj Deen K, Haider W, Asselin E, Shabib I. Corrosion behavior and biocompatibility of additively manufactured 316L stainless steel in a physiological environment: the effect of citrate ions. *Addit Manuf.* 2020;34:101237.
- Atapour M, Wang X, Färnlund K, Odnevall Wallinder I, Hedberg Y. Corrosion and metal release investigations of selective laser melted 316L stainless steel in a synthetic physiological fluid containing proteins and in diluted hydrochloric acid. *Electrochim Acta.* 2020;354:136748.
- Duan Z, Man C, Dong C, et al. Pitting behavior of SLM 316L stainless steel exposed to chloride environments with different aggressiveness: pitting mechanism induced by gas pores. *Corros Sci.* 2020;167:108520.
- Kale AB, Kim BK, Kim DI, Castle EG, Reece M, Choi SH. An investigation of the corrosion behavior of 316L stainless steel fabricated by SLM and SPS techniques. *Mater Charact.* 2020; 163:110204.
- Nakhaie D, Imani A, Autret M, Schaller RF, Asselin E. Critical pitting temperature of selective laser melted 316L stainless steel: a mechanistic approach. *Corros Sci.* 2021;185:109302.
- Mower TM, Long MJ. Mechanical behavior of additive manufactured, powder-bed laser-fused materials. *Mater Sci Eng A.* 2016;651:198-213.
- Zhang M, Sun CN, Zhang X, et al. Fatigue and fracture behaviour of laser powder bed fusion stainless steel 316L: influence of processing parameters. *Mater Sci Eng A.* 2017;703:251-261.
- Spierings AB, Starr TL, Wegener K. Fatigue performance of additive manufactured metallic parts. *Rapid Prototyp J.* 2013; 19:88-94.
- Kumar P, Jayaraj R, Suryawanshi J, Satwik UR, McKinnell J, Ramamurthy U. Fatigue strength of additively manufactured 316L austenitic stainless steel. *Acta Mater.* 2020;199:225-239.
- Montero-Sistiaga ML, Godino-Martinez M, Boschmans K, Kruth JP, Van Humbeeck J, Vanmeensel K. Microstructure evolution of 316L produced by HP-SLM (high power selective laser melting). *Addit Manuf.* 2018;23:402-410.
- Bahl S, Mishra S, Yazar KU, Kola IR, Chatterjee K, Suwas S. Non-equilibrium microstructure, crystallographic texture and morphological texture synergistically result in unusual

- mechanical properties of 3D printed 316L stainless steel. *Addit Manuf.* 2019;28:65-77.
21. Yin S, Yan X, Jenkins R, et al. Hybrid additive manufacture of 316L stainless steel with cold spray and selective laser melting: microstructure and mechanical properties. *J Mater Process Technol.* 2019;273:116248.
  22. Man C, Duan Z, Cui Z, et al. The effect of sub-grain structure on intergranular corrosion of 316L stainless steel fabricated via selective laser melting. *Mater Lett.* 2019;243:157-160.
  23. Yu J, Kim D, Ha K, Jeon JB, Lee W. Strong feature size dependence of tensile properties and its microstructural origin in selectively laser melted 316L stainless steel. *Mater Lett.* 2020; 275:128161.
  24. Song Y, Sun Q, Guo K, Wang X, Liu J, Sun J. Effect of scanning strategies on the microstructure and mechanical behavior of 316L stainless steel fabricated by selective laser melting. *Mater Sci Eng A.* 2020;793:139879.
  25. Dryepondt S, Nandwana P, Fernandez-Zelaia P, List F. Microstructure and high temperature tensile properties of 316L fabricated by laser powder-bed fusion. *Addit Manuf.* 2021;37: 101723.
  26. Deev AA, Kuznetsov PA, Petrov SN. Anisotropy of mechanical properties and its correlation with the structure of the stainless steel 316L produced by the SLM method. In: *Physics Procedia.* Vol 83. Elsevier B.V.; 2016:789-796.
  27. Salman OO, Gammer C, Chaubey AK, Eckert J, Scudino S. Effect of heat treatment on microstructure and mechanical properties of 316L steel synthesized by selective laser melting. *Mater Sci Eng A.* 2019;748:205-212.
  28. Zhang Z, Chu B, Wang L, Lu Z. Comprehensive effects of placement orientation and scanning angle on mechanical properties and behavior of 316L stainless steel based on the selective laser melting process. *J Alloys Compd.* 2019;791:166-175.
  29. Shi W, Liu Y, Shi X, Hou Y, Wang P, Song G. Beam diameter dependence of performance in thick-layer and high-power selective laser melting of Ti-6Al-4V. *Materials (Basel).* 2018;11:1237.
  30. Wang X, Zhao L, Fuh JYH, Lee HP. Experimental characterization and micromechanical-statistical modeling of 316L stainless steel processed by selective laser melting. *Comput Mater Sci.* 2020;177:109595.
  31. Li H, Ramezani M, Li M, Ma C, Wang J. Effect of process parameters on tribological performance of 316L stainless steel parts fabricated by selective laser melting. *Manuf Lett.* 2018;16: 36-39.
  32. Huang Y, Yang S, Gu J, et al. Microstructure and wear properties of selective laser melting 316L. *Mater Chem Phys.* 2020;254: 123487.
  33. Shin WS, Son B, Song W, et al. Heat treatment effect on the microstructure, mechanical properties, and wear behaviors of stainless steel 316L prepared via selective laser melting. *Mater Sci Eng A.* 2021;806:140805.
  34. Shamsujjoha M, Agnew SR, Fitz-Gerald JM, Moore WR, Newman TA. High strength and ductility of additively manufactured 316L stainless steel explained. *Metall Mater Trans A Phys Metall Mater Sci.* 2018;49:3011-3027.
  35. Voisin T, Forien JB, Perron A, et al. New insights on cellular structures strengthening mechanisms and thermal stability of an austenitic stainless steel fabricated by laser powder-bed-fusion. *Acta Mater.* 2021;203:116476.
  36. Chen L, Liu W, Song L. A multiscale investigation of deformation heterogeneity in additively manufactured 316L stainless steel. *Mater Sci Eng A.* 2021;820:141493.
  37. Li Z, Voisin T, McKeown JT, et al. Tensile properties, strain rate sensitivity, and activation volume of additively manufactured 316L stainless steels. *Int J Plast.* 2019;120:395-410.
  38. van Nuland TFW, van Dommelen JAW, Geers MGD. Microstructural modeling of anisotropic plasticity in large scale additively manufactured 316L stainless steel. *Mech Mater.* 2021;153: 103664.
  39. Solberg K, Guan S, Razavi SMJ, Welo T, Chan KC, Berto F. Fatigue of additively manufactured 316L stainless steel: the influence of porosity and surface roughness. *Fatigue Fract Eng Mater Struct.* 2019;42:2043-2052.
  40. Andreau O, Pessard E, Koutiri I, et al. A competition between the contour and hatching zones on the high cycle fatigue behaviour of a 316L stainless steel: analyzed using X-ray computed tomography. *Mater Sci Eng A.* 2019;757:146-159.
  41. Elangeswaran C, Cutolo A, Muralidharan GK, et al. Effect of post-treatments on the fatigue behaviour of 316L stainless steel manufactured by laser powder bed fusion. *Int J Fatigue.* 2019; 123:31-39.
  42. Bergant M, Werner T, Madia M, Yawny A, Zerbst U. Short crack propagation analysis and fatigue strength assessment of additively manufactured materials: an application to AISI 316L. *Int J Fatigue.* 2021;151:106396.
  43. Murphy-Leonard AD, Pagan DC, Callahan PG, Heinkel ZK, Jasien CE, Rowenhorst DJ. Investigation of porosity, texture, and deformation behavior using high energy X-rays during in-situ tensile loading in additively manufactured 316L stainless steel. *Mater Sci Eng A.* 2021;810:141034.
  44. Zhou J, Reira D, Sun Z, Kanouté P. Comparative study of the effects of surface mechanical attrition treatment and conventional shot peening on low cycle fatigue of a 316L stainless steel. *Surf Coatings Technol.* 2018;349:556-566.
  45. Mazánová V, Heczko M, Škorík V, Chlupová A, Polák J, Kruml T. Microstructure and martensitic transformation in 316L austenitic steel during multiaxial low cycle fatigue at room temperature. *Mater Sci Eng A.* 2019;767:138407.
  46. Yu CH, Leicht A, Peng RL, Moverare J. Low cycle fatigue of additively manufactured thin-walled stainless steel 316L. *Mater Sci Eng A.* 2021;821:141598.
  47. Riemer A, Leuders S, Thöne M, Richard HA, Tröster T, Niendorf T. On the fatigue crack growth behavior in 316L stainless steel manufactured by selective laser melting. *Eng Fract Mech.* 2014;120:15-25.
  48. Beausir B, Fundenberger JJ. ATEX©-analysis tools for electron and X-ray diffraction. 2015.
  49. Choo H, Sham KL, Bohling J, et al. Effect of laser power on defect, texture, and microstructure of a laser powder bed fusion processed 316L stainless steel. *Mater Des.* 2019;164:107534.
  50. Andreau O, Koutiri I, Peyre P, et al. Texture control of 316L parts by modulation of the melt pool morphology in selective laser melting. *J Mater Process Technol.* 2019;264:21-31.
  51. Sun S-H, Ishimoto T, Hagihara K, Tsutsumi Y, Hanawa T, Nakano T. Excellent mechanical and corrosion properties of austenitic stainless steel with a unique crystallographic lamellar microstructure via selective laser melting. *Scr Mater.* 2019; 159:89-93.

52. Zhong Y, Liu L, Wikman S, Cui D, Shen Z. Intragranular cellular segregation network structure strengthening 316L stainless steel prepared by selective laser melting. *J Nucl Mater.* 2016; 470:170-178.
53. Pillot S. Fusion laser sélective de lit de poudres métalliques. *Tech l'Ingenieur.* 2016;45:199-203.
54. Tolosa I, Garciandía F, Zubiri F, Zapiain F, Esnaola A. Study of mechanical properties of AISI 316 stainless steel processed by “selective laser melting”, following different manufacturing strategies. *Int J Adv Manuf Technol.* 2010;51:639-647.
55. Kuznetsov PA, Zisman AA, Petrov SN, Goncharov IS. Structure and mechanical properties of austenitic 316L steel produced by selective laser melting. *Russ Metall.* 2016;2016:930-934.
56. Liverani E, Toschi S, Ceschini L, Fortunato A. Effect of selective laser melting (SLM) process parameters on microstructure and mechanical properties of 316L austenitic stainless steel. *J Mater Process Technol.* 2017;249:255-263.
57. Mu P, Aubin V, Alvarez-Armas I, Armas A. Influence of the crystalline orientations on microcrack initiation in low-cycle fatigue. *Mater Sci Eng A.* 2013;573:45-53.
58. Guerchais R. Influence d'accidents geometriques et du mode de chargement sur le comportement en fatigue a grand nombre de cycles d'un acier inoxydable austenitique 316L;2014.
59. Uhlmann E, Fleck C, Gerlitzky G, Faltin F. Dynamical fatigue behavior of additive manufactured products for a fundamental life cycle approach. *Procedia CIRP.* 2017;61:588-593.
60. Kamaya M. A procedure for estimating Young's modulus of textured polycrystalline materials. *Int J Solids Struct.* 2009;46: 2642-2649.
61. Maity T, Chawake N, Kim JT, Eckert J, Prashanth KG. Anisotropy in local microstructure—does it affect the tensile properties of the SLM samples? *Manuf Lett.* 2018;15:33-37.
62. Robert C, Mareau C. A comparison between different numerical methods for the modeling of polycrystalline materials with an elastic-viscoplastic behavior. *Comput Mater Sci.* 2015;103: 134-144.
63. Huntington HB. The elastic constants of crystals. *Solid State Phys-Adv Res Appl.* 1958;7:213-351.

**How to cite this article:** Liang X, Hor A, Robert C, Salem M, Morel F. Correlation between microstructure and cyclic behavior of 316L stainless steel obtained by Laser Powder Bed Fusion. *Fatigue Fract Eng Mater Struct.* 2022;45(5): 1505-1520. doi:10.1111/ffe.13684